Lamb wave excitation and propagation in elastic plates with surface obstacles: proper choice of central frequencies

Evgeny Glushkov[1], Natalia Glushkova[1], Rolf Lammering[2], Artem Eremin[1] and Mirko N. Neumann[2]

[1] Kuban State University, Krasnodar 350040, Russia

[2] Institute of Mechanics, Helmut-Schmidt-University/University of the Federal Armed Forces Hamburg, D-22043 Hamburg, Germany

E-mail: `evg@math.kubsu.ru, rolf.lammering@hsu-hh.de`

Abstract. Experimental and theoretical investigations of Lamb wave excitation and sensing using piezo patch transducers and laser vibrometer technique have been performed, aiming at the development of adequate mathematical and computer models for the interpretation of sensing data and for the choice of optimal parameters for structural health monitoring. The proposed models are validated by experimental results. Furthermore, a methodology is presented which allows for the determination of central frequencies at which maximal values of the structural response spectrum can be expected in case of wave propagation monitoring with laser vibrometry.

1. Introduction

The development of structural health monitoring systems (SHM) which allow for inspection of large areas of layered structures is an important issue in actual research. Ultra-acoustic guided waves, especially Lamb waves, offer an attractive solution for SHM systems [1, 2, 3, 4]. Lamb waves can propagate along shell and plate structures over long distances as well as through their thickness and may be reflected by any defects. In recent years thin piezoelectric ceramic wafers which are applied to the structure for wave generation and signal acquisition became widely used for investigations of Lamb waves. These piezoelectric actuators and sensors are cheap, easy to use and can also become an integrated part of the monitored structure.

The definition of a proper model of the piezoactuator action on the elastic host structure is an important issue in theoretical investigations of piezoelectrically induced Lamb wave propagation. This action can be modeled using approximate pin-force models [5] or through the strict solution of dynamic contact problems for thin

piezoelectric elastic patches interacting with the underlying elastic structure [6, 7]. For frequency-thickness product values below 800 kHz-mm theoretical and experimental investigations of the simplified model applicability could be found in [8, 9, 10]. In these papers a very good coincidence between experimental and computed piezosensor response amplitudes is presented for a broad range of frequencies and different shapes of piezoactuators. A comparison between experimental and theoretical sensor response time domain signals for certain central frequencies is also given there.

Criteria for the selection of a proper central excitation frequency are of particular interest in structural health monitoring. This parameter strongly depends on the actuator size, material properties and signal sensing technique. In case of piezoelectric transducers catching in-plane motion [8] and thus being sensitive to both symmetric and antisymmetric modes, extensive numerical and experimental studies of the problem were carried out for plates fabricated from isotropic materials (aluminium alloys) based on simplified actuator model [11, 12]. Based on these investigations a conception of 'sweet spot' frequencies has been proposed. At such central frequencies the maximum peak of wave amplitude ratio between the s_0 and a_0 modes in the sensor output is reached. It is expected that such selection could minimize interference between different Lamb waves and thus lead to easier sensor signal interpretation. Thorough investigations of this phenomena in application to notch and crack detection in an aluminium narrow-strip were performed in [13].

Recently, laser vibrometer technique has been identified as a powerful tool for Lamb wave sensing. Basically, one scanning device allows to measure the out-of-plane velocity utilizing the Doppler shift phenomenon [9, 10, 14]. At relatively low frequencies (below the first cut-off frequency for a free elastic layer) the antisymmetric mode is mainly visible, since in general, the s_0 mode shows a significantly smaller velocity amlitude than the a_0 mode. Therefore another approach for the proper selection of the excitation frequency and for the identification of so-called *sweet spots* is needed which is different from the direct use of piezoelectric sensors. As a solution of this problem it is proposed to perform signal excitation at central frequencies which are equal or close to those where local peaks of a_0 mode response are achieved.

Unfortunately, in many practical applications the mechanical properties of the investigated structure are either unknown or rather complex, for example, in the case of anisotropic material. This circumstance is a severe obstacle to the theoretical finding of 'sweet spot' or 'local peak' frequencies. On the other hand, the experimental determination of these frequencies can be time-consuming. Therefore, theoretical investigations of wave patterns associated with different excitation frequencies are of particular importance.

In the present work such theoretical investigations, validated by experimental measurements, are performed relying on an analytically-based computer model. The paper is aimed at comparative studying of 'sweet spot' and 'local peak' excitation regimes and, indirectly, at the demonstration of capabilities of the model developed.

The paper is structured as follows. At first the experimental setup is described in

section 2, which is continued by the mathematical model description in section 3. Then the experimental and theoretical results are discussed in section 4, firstly with regard to the model validation and then in view of a proper choice of excitation frequencies.

2. Experimental setup

Two aluminium plates (Young's modulus $E = 70$ GPa, Poisson's ratio $\nu = 0.33$, density $\rho = 2700$ kg/m^3) are used in the experiments. The smaller one ($\approx 300 \times 600 \times 1$ mm^3) is used to investigate the propagating field excited by the piezoceramic actuator. The bigger one ($\approx 1000 \times 1000 \times 1$ mm^3) serves as a test specimen for experiments with surface obstacles. Each plate is equipped with a single, circular, vertically polarized piezoceramic actuator (diameter $D = 16$ mm, thickness $b = 0.25$ mm). The actuators are adhered to the surface of the plates with superglue (Loctite 401). The plates are placed on a ridged lightweight foam.

A two-cycle sine-windowed sine toneburst with central frequencies at $50, 100$ and 170 kHz is applied to the actuators at both specimens. For this purpose a Tektronix AFG 3022B two-channel arbitrary signal generator was used. The generated signal is amplified (Develogic WBHV 2A600 amplifier) before it is applied to the actuator.

The velocity field of the propagating wave is captured by means of a Polytec PSV-400 scanning laser vibrometer coupled with a Tektronix TDS 1012B two-channel digital storage oscilloscope. The scanning head of PSV-400 system is placed 1.527m above the plate. In order to improve the reflection of the laser beam and to minimize the signal to noise ratio a thin reflective film is glued to the surface of the plates in the area of observation.

Two powerful permanent magnets in the shape of thick-walled cylinders are used as surface obstacles (inner radius $a_1 = 3$ mm, outer radius $a_2 = 7.5$ mm, mass $m = 0.0065$ kg). They are fixed (and can easily be removed) oppositely at both sides of the plate and they can be located at an arbitrary position.

3. Mathematical model

3.1. Statement of the problem and integral representations

In order to simulate numerically the Lamb wave fields generated and measured at the experimental setup described above, let us consider a linearly elastic isotropic layer of thickness H, occupying in the Cartesian coordinates $\mathbf{x} = (x, y, z)$, with the origin put at the center of circular piezopatch contact area Ω, a semi-infinite domain $D : \{-\infty < x, y < \infty, -H \leq z \leq 0\}$ (figure 1). (Thus, wave reflection from the plate edges is not considered.) Time-dependent displacements of the layer $\mathbf{u}(\mathbf{x}, t)$ are routinely expressed via the time-harmonic oscillations (frequency spectrum) $\mathbf{u}(\mathbf{x}, \omega)e^{-i\omega t}$

using the inverse Fourier transform $\mathcal{F}_t^{-1}$:

$$\mathbf{u}(\mathbf{x}, t) = \mathcal{F}_t^{-1}[\mathbf{u}(\mathbf{x}, \omega)] = \frac{1}{2\pi} \int\limits_{-\infty}^{\infty} \mathbf{u}(\mathbf{x}, \omega) e^{-i\omega t} d\omega. \tag{3.1}$$

Hereinafter, when not confusing, we use the same symbols for time-domain functions and their frequency spectra, distinguishing them just by the second argument, e.g. $\mathbf{u}(\mathbf{x}, t)$ and $\mathbf{u}(\mathbf{x}, \omega)$; if it is clear from the context, some of arguments, as well as harmonic factor $e^{-i\omega t}$, may be omitted. To distinguish column vectors from rows, the former are denoted by braces, while the latter are in parenthesis: $\mathbf{u} = \{u_x, u_y, u_z\} = (u_x, u_y, u_z)^T$.
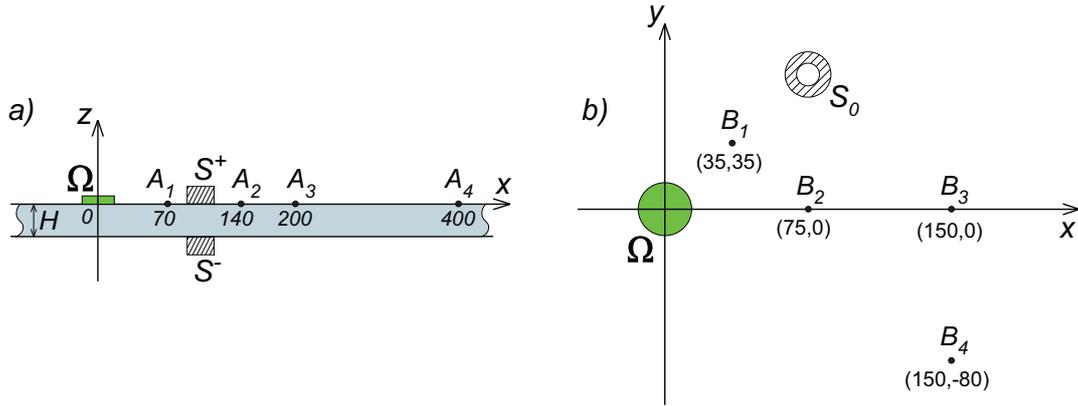
Figure 1. Side and top view of the elastic plate with circular piezoelectric actuator, ring-shaped obstacles and test points A_k and B_m.

The displacement complex amplitude $\mathbf{u}(\mathbf{x}, \omega)$ obeys the Lamé-Navier equation

$$(\lambda + \mu)\nabla\operatorname{div}\mathbf{u} + \mu\Delta\mathbf{u} + \rho\omega^2\mathbf{u} = 0, \quad \mathbf{x} \in D, \tag{3.2}$$

where λ, μ and ρ are Lamé elastic constants and material density, respectively. The layer surfaces $z = 0$ and $z = -H$ are stress-free, except the patch-layer contact area $\Omega : 0 \leq r \leq a$, $z = 0$ and the annular contact areas S^+ and S^- of two obstacles (magnets) symmetrically located on the surfaces $z = 0$ and $z = -H$, respectively, $(x, y) \in S_0$: $a_1 \leq r_s \leq a_2$; here $r = \sqrt{x^2 + y^2}$ and $r_s = \sqrt{(x - x_s)^2 + (y - y_s)^2}$, (x_s, y_s) is the center of the scattering domains $S^{\pm}$. Since the obstacles are relatively heavy and their vibration, as compared with the free-surface displacements, is very small, they are assumed to be immovable.

Hence, the boundary conditions are stated in the form

$$\boldsymbol{\tau}|_{z=0} = \begin{cases} \mathbf{q}_0, & (x, y) \in \Omega \\ \mathbf{q}_s^+, & (x, y) \in S^+ \\ 0, & \text{elsewhere} \end{cases} \quad \text{and} \quad \boldsymbol{\tau}|_{z=-H} = \begin{cases} \mathbf{q}_s^-, & (x, y) \in S^- \\ 0, & \text{elsewhere} \end{cases} \tag{3.3}$$

$$\mathbf{u}|_{z=0} = 0, \ (x, y) \in S^+ \quad \text{and} \quad \mathbf{u}|_{z=-H} = 0, \quad (x, y) \in S^-. \tag{3.4}$$

Here $\boldsymbol{\tau} = \{\tau_{xz}, \tau_{yz}, \sigma_z\}$ is a traction vector at a horizontal surface $z = \text{const}$, $\mathbf{q}_0(x, y)$ is an axially symmetric surface traction produced in the area Ω by the circular patch

actuator, which is assumed to be prescribed, while $\mathbf{q}_s^\pm(x, y)$ are unknown contact stresses under the obstacles; the latter have to be obtained via the contact problem solution.

For the infinite domain D boundary conditions $(3.3) - (3.4)$ have to be supplemented by certain radiation conditions at infinity. If the medium possesses a small wave attenuation ε, the condition of wave amplitude tending to zero

$$\mathbf{u} \to 0 \quad \text{as} \quad r = \sqrt{x^2 + y^2} \to \infty \tag{3.5}$$

completes the boundary value problem (BVP) $(3.1) - (3.4)$. For an ideally elastic medium it is supplemented by the principle of limiting absorption [15], which means that the solution for an ideal medium is the limit of the unique solution of the corresponding problem for a medium with attenuation as $\varepsilon \to 0$.

To derive efficient algorithms for a fast computer simulation of wave fields generated in a laminate waveguide by a surface load $\mathbf{q}$, we rely on the wave field representation via the convolution of Green's matrix $k(\mathbf{x})$ for a layered structure considered with the load vector $\mathbf{q}$ applied to a surface area S:

$$\mathbf{u}(\mathbf{x}) = \iint\limits_S k(\mathbf{x} - \boldsymbol{\xi})\mathbf{q}(\boldsymbol{\xi})d\boldsymbol{\xi}, \tag{3.6}$$

which is a traditional start point in the context of the analytically based integral approach developed [16].

Conventionally elastodynamic problems are brought to boundary integral equations (BIEs) using the matrix of fundamental solutions (Green matrix) $g(\mathbf{x})$ derived for an infinite homogeneous elastic space. The discretization of such BIEs yields classical boundary element (BE) approximations [17], which, however, are not advantageous for thin structures, since the BEs have to be allocated along all the surfaces. The matrix $k(\mathbf{x})$ is also a matrix of fundamental solutions, but, as distinct from $g(\mathbf{x})$, it is derived for the waveguide considered accounting for boundary conditions on the plane-parallel surfaces. Specifically, the columns $\mathbf{k}_j$ of this matrix are the solutions $\mathbf{u}_j$ associated with the three point loads

$$\boldsymbol{\tau}|_{z=0} = \mathbf{i}_j \delta(x, y), \quad j = 1, 2, 3 \tag{3.7}$$

directed along the coordinate unit vectors $\mathbf{i}_j$, while the rest of boundary conditions is homogeneous. In that way, integral representations like (3.6) satisfy identically all homogeneous boundary conditions at the plane-parallel surfaces, so that the area of integration and further discretization S is relatively small.

Using the Fourier transform $\mathcal{F}_{xy}$ applied to the equations and boundary conditions with respect to the horizontal coordinates x and y, the matrix k is expressed via its Fourier symbol K:

$$k(\mathbf{x}) = \mathcal{F}_{xy}^{-1}[K] \equiv \frac{1}{4\pi^2} \int\limits_{\Gamma_1} \int\limits_{\Gamma_2} K(\alpha_1, \alpha_2, \alpha, z)e^{-i(\alpha_1 x + \alpha_2 y)}d\alpha_1 d\alpha_2. \tag{3.8}$$

The integration paths Γ_1 and Γ_2 go in the complex planes α_1, α_2 along the real axes $\operatorname{Im} \alpha_n = 0$, $n = 1, 2$, deviating from them for bypassing real poles of the matrix K elements. The direction of deviation is governed by the principle of limiting absorption.

In the conventional notation (e.g., see [18]) the symbol K for an isotropic layered waveguide may be written in the following form

$$K = \begin{bmatrix} -i(\alpha_1^2 M + \alpha_2^2 N) & -i\alpha_1^2\alpha_2^2(M-N) & -i\alpha_1 P \\ -i\alpha_1^2\alpha_2^2(M-N) & -i(\alpha_1^2 N + \alpha_2^2 M) & -i\alpha_2 P \\ \alpha_1 S & \alpha_2 S & R \end{bmatrix}, \qquad (3.9)$$

where functions M, N, P, R, S depend only on $\alpha = \sqrt{\alpha_1^2 + \alpha_2^2}$ and z. For a homogeneous elastic layer they can be derived in an explicit analytical form (see Appendix). Conformably with eq. (3.8), convolution (3.6) can be brought to the equivalent path integral form

$$\mathbf{u}(\mathbf{x}) = \frac{1}{4\pi^2} \int\limits_{\Gamma_1} \int\limits_{\Gamma_2} K(\alpha_1, \alpha_2, \alpha, z) \mathbf{Q}(\alpha_1, \alpha_2) e^{-i(\alpha_1 x + \alpha_2 y)} d\alpha_1 d\alpha_2, \qquad (3.10)$$

where $\mathbf{Q} = \mathcal{F}_{xy}[\mathbf{q}]$.

Representations (3.6) and (3.10) are valid for a load $\mathbf{q}$ given at the upper surface $z = 0$, while for loads applied to the lower surface $z = -H$ (for $\mathbf{q}_s^-$ in the case) similar representation with the matrix $k^-(\mathbf{x}) = \mathcal{F}_{xy}^{-1}[K^-]$ is employed. Its elements K_{ij}^- are expressed through the K elements: $K_{ij}^-(z) = (-1)^{i+j-1}K_{ij}(-z-H)$, $i, j = 1, 2$.

Thus, the solution of BVP (3.2) – (3.5) may be written in the form

$$\mathbf{u} = \mathbf{u}_0 + \mathbf{u}_{sc}, \quad \mathbf{u}_{sc} = \mathbf{u}_{sc}^+ + \mathbf{u}_{sc}^-$$

$$\mathbf{u}_0(\mathbf{x}) = \iint\limits_{\Omega} k(x-\xi, y-\eta, z)\mathbf{q}_0(\xi, \eta)d\xi d\eta \qquad (3.11)$$

$$\mathbf{u}_{sc}^\pm(\mathbf{x}) = \iint\limits_{S^\pm} k^\pm(x-\xi, y-\eta, z)\mathbf{q}_s^\pm(\xi, \eta)d\xi d\eta, \quad (k^+ \equiv k)$$

where $\mathbf{u}_0$ is the incident field generated by the load $\mathbf{q}_0$ in the infinite plate without obstacles, while $\mathbf{u}_{sc}^\pm$ are fields scattered by obstacles.

3.2. Incident field

Under applied voltage $V e^{-i\omega t}$ the circular piezoelectric patch expands from and contracts to the center $r = 0$ in the radial directions. Therefore, with relatively thin and flexible patches bonded to a layer, the vertical and angular components σ_{zz} and $\tau_{\varphi z}$ of the generated contact stresses are negligible, so that only the radial component τ_{rz} is worth to be taken into account. Thus, in the cylindrical coordinates (r, φ, z): $x = r\cos\varphi, y = r\sin\varphi, r = \sqrt{x^2 + y^2}, 0 \le \varphi \le 2\pi$, the traction vector $\mathbf{q}_0 = \{q_r, q_\varphi, q_z\}$ may be taken in the form $\mathbf{q}_0 = \{p, 0, 0\}$ with an independent of φ shape function $p(r)$ for the radial contact traction. In general, this function is unknown and so it has to be obtained via solution of a patch-layer contact problem just as it was performed for strip patch actuators [7] or using the Galerkin approach, similarly as for the scattered field $\mathbf{u}_{sc}$ below.

However, at relatively low frequencies the contact stresses, exhibiting square-root singular concentration at the border of contact area $\partial\Omega$ [19], may be well approximated by the square-root function $p(r) = p_0/\sqrt{1 - (r/a)^2}$. Moreover, in regard to far-field

asymptotics of generated Lamb waves, the concentrated ring delta-like distribution of radial tensions along the border $p(r) = p_0\delta(r-a)$ may be successfully substituted for the patch action on the surface, similar to the pin-force models for strip and rectangular patch actuators [5, 20, 21]. Test calculations against experimental measurements carried out in the indicated works and in the cited therein ones, as well as comparisons with the results obtained via strict contact problem solution [7], have shown the applicability of delta-like approximations within a considerable part of the two-mode frequency range. It gave a ground to use such a model for the circular patch actuator employed, as well. Its validity has been confirmed by the experimental measurements presented below (see section 4).

With an axially symmetric load $q_r = p(r)$ the generated field $\mathbf{u}_0 = \{u_r, u_\varphi, u_z\}$, considered in cylindrical coordinates, is also axisymmetric. Actually, its components are expressed through q_r in terms of Fourier-Bessel integrals derived from eq. (3.10) via the change of variables $\alpha_1 = \alpha\cos\gamma$, $\alpha_2 = \alpha\sin\gamma$, $\alpha = \sqrt{\alpha_1^2 + \alpha_2^2}$, $0 \le \gamma \le 2\pi$, and the use of the integral representation for the Bessel functions J_n [22]

$$(\pm i)^n 2\pi J_n(r) = \int_0^{2\pi} e^{\pm i(r\cos(\varphi-\gamma)-n\gamma)}d\gamma.$$

As a result,

$$u_r(r,z) = -\tfrac{1}{2\pi}\int_{\Gamma_+} M(\alpha,z)P(\alpha)J_1(\alpha a)\alpha^3 d\alpha$$

$$u_\varphi(r,z) = 0 \tag{3.12}$$

$$u_z(r,z) = \tfrac{1}{2\pi}\int_{\Gamma_+} S(\alpha,z)P(\alpha)J_0(\alpha a)\alpha^2 d\alpha$$

where

$$P(\alpha) = 2\pi i \int_0^\infty p(r)J_1(\alpha r)r\,dr \tag{3.13}$$

is the Fourier-Bessel transform of the radial stress component q_r. In view of the ring δ-function property

$$2\pi\int_0^\infty f(r)\delta(r-a)r\,dr = f(a)$$

eq. (3.13) is reduced to the close analytical representation $P(\alpha) = p_0 i J_1(\alpha a)$, which is substituted in eq. (3.12) if a ring δ-source is considered. Functions M and S in (3.12) are those entering in the first column of matrix K (3.9); the contour Γ_+ results from Γ_1 and Γ_2 in line with the change of variables α_1 and α_2, it goes in the complex plane α along the real semi-axis $\mathrm{Re}\,\alpha \ge 0$, $\mathrm{Im}\,\alpha = 0$ deviating from it to bypass the real positive poles ζ_n of the functions M and S. The latter are roots of the characteristic equation

$$\Delta(\alpha,\omega) = 0 \quad\Rightarrow\quad \alpha = \zeta_n(\omega), \tag{3.14}$$

where Δ is the common denominator of these functions (see Appendix). In fact, it is the Lamb wave dispersion equation yielding wave numbers ζ_n for both antisymmetric and symmetric Lamb modes a_k and s_k, $k = 0, 1, 2, ...$ [23].

Using the residual technique, integrals (3.13) are brought to the series

$$
\begin{aligned}
u_r &= \sum_{n=1}^{\infty} a_n^{(1)}(z) H_1^{(1)}(\zeta_n r) \\
u_z &= \sum_{n=1}^{\infty} a_n^{(2)}(z) H_0^{(1)}(\zeta_n r)
\end{aligned}
\quad , \quad r > a
\tag{3.15}
$$

$$
\mathbf{a}_n = \{a_n^{(1)}, a_n^{(1)}\} = -\{i\zeta_n M_n(z), S_n(z)\} \zeta_n^2 P(\zeta_n)/2
$$

where $M_n = \operatorname{res} M(\alpha, z)|_{\alpha = \zeta_n}$, $S_n = \operatorname{res} S(\alpha, z)|_{\alpha = \zeta_n}$, $P(\zeta_n) = p_0 i J_1(\zeta_n a)$, $H_0^{(1)}$ and $H_1^{(1)}$ are cylindrical Hankel functions, exhibiting the far-field asymptotic behavior [22]

$$
H_m^{(1)}(\zeta_n r) = \sqrt{\frac{2}{\pi i \zeta_n r}} (-i)^m e^{i\zeta_n r} [1 + O(1/(\zeta_n r))], \quad |\zeta_n r| >> 1.
\tag{3.16}
$$

Poles ζ_n are supposed to be numbered in ascending order of their imaginary parts: $\operatorname{Im} \zeta_{n+1} \geq \operatorname{Im} \zeta_n$, so that the totally real ones go first.

Hence, at a fixed frequency ω there are a few first terms of series (3.15) associated with real poles that describe traveling Lamb waves propagating from the source in radial directions with the phase and group velocities $v_n = \omega/\zeta_n$ and $c_{g,n} = d\omega/d\zeta_n$. The vectors $\mathbf{a}_n$ are normal mode eigenforms coinciding to constant factors with those obtained from the BVP with homogeneous boundary conditions using the modal analysis technique. In contrast to the latter, $\mathbf{a}_n$ are uniquely fixed and via the factors $P(\zeta_n)$ they account for the information about the source; in particular, it allows one to analyze the source energy partition among the excited modes. The complex poles ζ_n occurring for $n \geq N_r + 1$ (N_r is a number of real poles) yield exponentially decaying normal modes with the amplitude decreasing as $e^{-|\operatorname{Im} \zeta_n| r}/\sqrt{|\zeta_n r|}$, $|\zeta_n r| \to \infty$. Therefore, series (3.15) are fast-converging ones, so as only one or two complex ζ_n are usually enough to keep their reasonably accurate truncation for all $r > r_0 > a$ with a rather not distant threshold value r_0. For distant r (e.g., for the points used in the experimental measurements) no complex ζ_n have been required to take into account at all.

The measurements have been carried out within the two-mode frequency range, in which only fundamental modes a_0 and s_0 can be excited ($N_r = 2$). In eq. (3.15) they are described by the terms associated with the two first poles (wave numbers) ζ_1 and ζ_2. The plots of their frequency dependencies (dispersion curves), as well as plots for group velocities are well-known, but for the clearness of further discussions they are depicted in figure 2 once again in both dimensionless and dimensional coordinates. The vertical dashed lines indicate the central frequencies f_i (and dimensionless ω_i) for which the results of measurements and calculations are presented below. To give an idea about the comparability of displacement components in the excited a_0 and s_0 modes, figure 3 displays dimensionless plots of the amplitudes of residuals $M_n(0)$ and $S_n(0)$, which control eigenvectors $\mathbf{a}_n$ in eq. (3.15). Since the difference is large, the plots are given in a logarithmic scale. One can see the overall dominance of the vertical component

of bending mode a_0 controlled by S_n (lower subplot), while the radial component of s_0 mode are expectedly larger than of a_0 one (upper subplot).
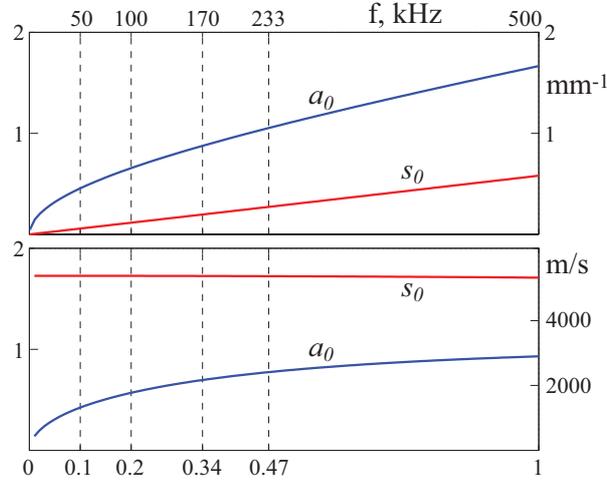
Figure 2. Dispersion curves of fundamental modes: wave numbers ζ_n (top) and group velocities $c_{g,n}$ (bottom) versus frequency.
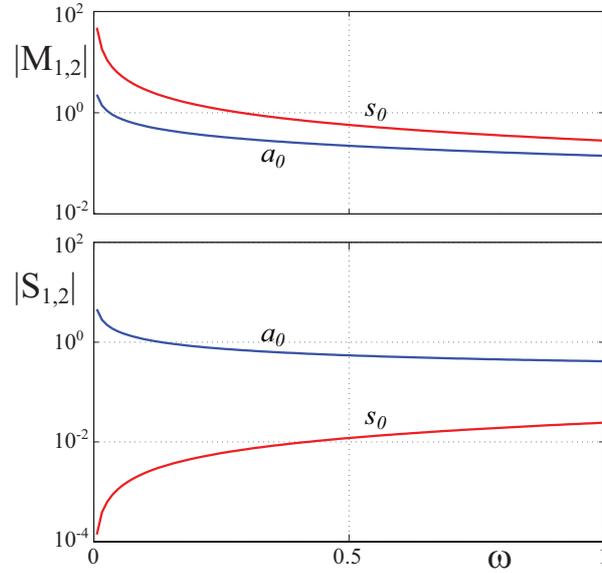
Figure 3. Residuals $M_n(0)$ and $S_n(0)$ vs. ω.

The dimensionless form are introduced by the choice of $l_0 = H$ as the unit of length, $v_0 = v_s$ as the unit of velocity and $\rho_0 = \rho$ as the unit of density. In these units the dimensionless angular frequency $\omega = 2\pi f H/v_s$, where f is dimensional frequency.

Specifically, for the plate under consideration

$$l_0 = 1\,\text{mm} = 10^{-3}\,\text{m} \qquad f_0 = v_0/l_0 = 3.122 \cdot 10^6\,\text{s}^{-1} = 3.122\,\text{MHz}$$
$$v_0 = 3122\,\text{m/s} \qquad t_0 = 1/f_0 = 0.32 \cdot 10^{-6}\,\text{s} = 0.32\,\mu\text{s}$$
$$\rho_0 = 2700\,\text{kg/m}^3 \qquad p_0 = \rho_0 v_0^2 l_0^2 = 2.63 \cdot 10^4\,\text{N}$$

Series representation of form (3.15) is valid for any axisymmetric shear tension $\tau_{rz} = p(r)$. If the load $\mathbf{q}$ is asymmetric, the generated field $\mathbf{u}_0$ may be approximated by a superposition of fields $\mathbf{u}_j$ excited by the point-wise δ-sources

$$\boldsymbol{\tau}|_{z=0} = \mathbf{q}_j \delta(\mathbf{x} - \mathbf{x}_j), \quad \mathbf{x}_j = (x_j, y_j, 0), \ j = 1, 2, ..., N_q \tag{3.17}$$

distributed in the load area [18]. Obviously, these wave fields $\mathbf{u}_j$ are expressed via the Green matrix $k(\mathbf{x})$ without any integration over the load area:

$$\mathbf{u}(\mathbf{x}) \approx \sum_{j=1}^{N_q} \mathbf{u}_j(\mathbf{x}), \quad \mathbf{u}_j(\mathbf{x}) = k(\mathbf{x} - \mathbf{x}_j)\mathbf{q}_j. \tag{3.18}$$

This sum itself may be treated as a cubature approximation for the convolution integral (3.6).

The same way as eq. (3.15), every $\mathbf{u}_j$ can also be represented explicitly in terms of normal modes in the local cylindrical coordinates (r_j, φ_j, z) centered at the source points $\mathbf{x}_j$. For example, instead of the ring δ-source used in series representation (3.15), the load approximation by a set of the point-wise δ-sources allocated evenly along the border $r = a$ has also been used for test calculations. The validity of such approximation is illustrated by figure 4, in which the normalized vertical amplitude $|u_z|$ calculated at the surface point $\mathbf{x} = (100, 0, 0)$ is plotted versus the dimensionless radius a of the source area Ω. Solid lines are for the results obtained using eq. (3.15), while the markers show the values obtained via approximation (3.18) with $N_q = 48$ point sources (3.17) located at the points $\mathbf{x}_j = a\{\cos\theta_j, \sin\theta_j, 0\}$ and producing radial shear tensions $\mathbf{q}_j = p_0\{\cos\theta_j, \sin\theta_j, 0\}/N_q$, $\theta_j = 2\pi j/N_q$, $j = 1, 2, ..., N_q$; $\omega = 0.5$.
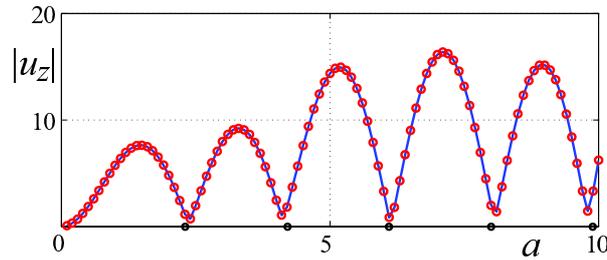
Figure 4. Comparison of source models at $\omega = 0.5$.

Besides the validation of expansions (3.18), this figure visually shows that with certain patch sizes the laser-registered displacement component u_z becomes very small. Obviously, it occurs when the source factor $P(\zeta_1)$, controlling the dominant a_0 amplitude, is equal to zero, i.e. when

$$\zeta_1 a = j_k \quad \text{or} \quad a/\lambda_1 = j_k/(2\pi), \quad k = 1, 2, ..., \tag{3.19}$$

where j_k are the Bessel function zeros: $J_1(j_k) = 0$, $\lambda_1 = 2\pi/\zeta_1$ is the wavelength of bending mode a_0. The radii $a_k = j_k/\zeta_1$ hitting upon conditions (3.19) are marked in figure 4 by the dark points on the axis a. Apparently, with laser vibrometer based measurements, one ought to avoid patch sizes and central frequencies falling into this condition.

3.3. Scattered field

The field $\mathbf{u}_{sc}$ may be evaluated by the same way as $\mathbf{u}_0$, but only after the unknown contact stresses $\mathbf{q}_s^\pm$ have been obtained from the boundary integral equations (BIEs). The diffraction problem is reduced to the BIEs

$$\mathcal{K}\mathbf{q}_s = \mathbf{f}, \quad \mathbf{x} \in S^\pm \tag{3.20}$$

by the substitution of fields (3.11) into boundary conditions (3.4). Here $\mathbf{q}_s = \{\mathbf{q}_s^+, \mathbf{q}_s^-\}$ and $\mathbf{f} = -\{\mathbf{u}_0^+, \mathbf{u}_0^-\}$ are generalized six-component vectors of unknown contact stresses and known incident displacements in the domains S^+ and S^-; $\mathcal{K} = [\mathcal{K}_{ij}]_{i,j=1}^2$ is a 6×6 matrix integral operator formed from the 3×3 matrix integral operators $\mathcal{K}_{ij}$ of the right parts of $\mathbf{u}_{sc}^\pm$ representations (3.11) with $\mathcal{K}_{i1}$ and $\mathcal{K}_{i2}$ expressed via k^+ and k^-, respectively, at $z = 0$ ($i = 1$) and $z = -H$ ($i = 2$), $(x, y) \in S_0$.

Since the distribution of contact stresses induced by the incident waves $\mathbf{u}_0$ is non-axially symmetric, it is convenient to use for BIE solution the expansions in terms of δ-like axially-symmetric (radial) basis functions $\psi_j(x, y) = \psi(\frac{x-x_j}{h}, \frac{y-y_j}{h})$ centered at the nodes (x_j, y_j) covering evenly the domain of integration S_0 with a spacing h; $\psi(x, y) = \psi(r)$ is a radial shape function, its δ-like property means that $\psi(x/h, y/h)/h^2 \to \delta(x, y)$ as $h \to 0$. The variational Galerkin scheme, i.e. the substitution of the expansion

$$\mathbf{q}_s \approx \mathbf{q}_N(x, y) = \sum_{j=1}^N \mathbf{c}_j \psi_j(x, y), \quad \mathbf{c}_j = \{\mathbf{c}_j^+, \mathbf{c}_j^-\} \tag{3.21}$$

into eq. (3.20) and projection of the discrepancy $\mathcal{K}\mathbf{q}_N - \mathbf{f}$ onto the same basis ψ_i, leads to the linear algebraic system with respect to unknown expansion coefficients $\mathbf{c}_j$:

$$\sum_{j=1}^N b_{ij}\mathbf{c}_j = \mathbf{f}_i, \quad i = 1, 2, ..., N$$
$$b_{ij} = (\mathcal{K}\psi_j, \psi_i)_{L_2}, \quad \mathbf{f}_i = (\mathbf{f}, \psi_i)_{L_2}.$$

The use of radial shape functions $\psi(r)$ allows one to avoid numerical integration of multifold singular integrals for obtaining the system coefficients b_{ij} and $\mathbf{f}_i$ by bringing them to a one-fold form similar to path integrals (3.12). They may also be represented in terms of residuals from the poles ζ_n. As a result, the cost of matrix $B = [b_{ij}]$ and vector $\mathbf{f} = \{\mathbf{f}_1, \mathbf{f}_2, ..., \mathbf{f}_N\}$ compiling becomes less than of the system solution itself.

In line with expansion (3.21) the diffracted field $\mathbf{u}_{sc}$ is approximated by the sum of fields $\mathbf{u}_j^\pm$ radiated by the locally axisymmetric sources $\psi_j \mathbf{c}_j^\pm$ located in the areas $S^\pm$:

$$\mathbf{u}_{sc} \approx \sum_{j=1}^N (\mathbf{u}_j^+ + \mathbf{u}_j^-),$$

$$\mathbf{u}_j^\pm = \frac{h^2}{4\pi} \int_\Gamma K(i\partial/\partial x, i\partial/\partial y, \alpha, z) \mathbf{c}_j^\pm \Psi(\alpha h) H_0^{(1)}(\alpha r_j) \alpha d\alpha = \qquad (3.22)$$

$$= \frac{ih^2}{2} \sum_{n=1}^\infty \operatorname{res} K(i\partial/\partial x, i\partial/\partial y, \alpha, z)|_{\alpha=\zeta_n} \mathbf{c}_j^\pm \Psi(\zeta_n h) H_0^{(1)}(\zeta_n r_j) \zeta_n,$$

$$\Psi(\alpha) = \mathcal{F}_{xy}[\psi] = 2\pi \int_0^1 \psi(r) J_0(\alpha r) r dr, \quad r_j = \sqrt{(x-x_j)^2 + (y-y_j)^2}.$$

The derivatives $i\partial/\partial x$ and $i\partial/\partial y$ stand in the matrix K on the places of variables α_1 and α_2 in accordance with the general Fourier transform property

$$\mathcal{F}_{xy}\left[\frac{\partial^{p_1+p_2}}{\partial x^{p_1} \partial y^{p_2}} u(x,y)\right] = (-i\alpha_1)^{p_1}(-i\alpha_2)^{p_2} U(\alpha_1, \alpha_2).$$

They act on the Hankel function $H_0^{(1)}(\zeta_n r_j)$ yielding the Hankel functions again [22] so that no any derivatives actually remain in the final representation. For example,

$$-i\alpha_1 \;\rightarrow\; \frac{\partial}{\partial x} H_0^{(1)}(\zeta_n r_j) = -\zeta_n \cos\varphi_j H_1^{(1)}(\zeta_n r_j)$$

$$-\alpha_1^2 \;\rightarrow\; \frac{\partial^2}{\partial x^2} H_0^{(1)}(\zeta_n r_j) = \zeta_n^2 \cos^2\varphi_j\, H_0^{(1)}(\zeta_n r_j) - \zeta_n/r_j H_1^{(1)}(\zeta_n r_j)$$

$$\cos\varphi_j = (x-x_j)/r_j$$

Originally this approach has been proposed and proved its efficiency for dynamic contact problems with arbitrarily shaped contact domains, and then it has been extended for elastodynamic scattering problems, as well. The details of its implementation may be found in [16, 18] and papers mentioned therein. Therefore, we stop description at this point, just adding that for $\mathbf{u}_{sc}$ calculations below the bell-like shape function

$$\psi(r) = \begin{cases} \frac{2}{\pi}(1-r^2), & 0 \le r \le 1 \\ 0, & r > 1 \end{cases} \quad \text{with} \quad \Psi(\alpha) = 8J_2(\alpha)/\alpha^2$$

has been used.

4. Results and discussion

In this section we present at first the results of the theory-to-experiment comparisons validating the computer model developed, then we discuss rules for a proper choice of central excitation frequencies for a laser-based structural health monitoring following from the numerical analysis performed.

4.1. Model validation

To test the prediction ability of the mathematical model described above, there have been performed two series of experimental measurements. In the course of the first one the out-of-plane displacements $u_z(t)$ generated by the piezo patch source of radius $a = 8$ mm in the aluminium plate without obstacles were measured by the laser vibrometer and/or calculated at the points $A_k, k = 1, 2, 3, 4$, lying on the same with source surface $z = 0$ (figure 1). Apparently, this series dealt only with the incident field $\mathbf{u}_0$. In the second series, the signals $u_z(t)$ related to the total field $\mathbf{u} = \mathbf{u}_0 + \mathbf{u}_{sc}$ were calculated and measured in the points $B_m, m = 1, 2, 3, 4$ lying on the lower surface $z = -H$ (figure 1), as well as at a number of surface points in a rectangle area 100×100 mm^2 for compiling 2D scan-images illustrating Lamb wave diffraction by obstacles (e.g. figure 9 below). The source patch has been driven by the two-cycle sine-windowed sine excitation voltage signal

$$V(t) = \begin{cases} \sin(2\pi f_c t) \sin(\pi f_c t/2), & 0 \le t \le 2T \\ 0, & t > 2T \end{cases} \tag{4.1}$$

at the central frequencies $f_c = f_i$, $f_i = 50, 100$ and 170 kHz for $i = 1, 2$ and 3, respectively (in the dimensionless form at $\omega_c = 0.10, 0.20$ and 0.34; see figure 2); $T = 1/f_c$ is the period of sine cycle.

The results of the first series are presented in figures 5 – 7 displaying theoretical (solid lines) and experimental (dashed lines) signal patterns $u_z(t)$ related to Lamb waves excited with the central frequencies f_i specified above and registered at the points A_1 and A_2 (subplots (b) and (c), respectively). The amplitudes of the signals are normalized to their maximal absolute values. The subplots (a) of these figures show the dimensionless frequency spectrum amplitudes for the driving pulse ($|V(\omega)|$, solid line), for the plate displacement response on the δ-pulse $\boldsymbol{\tau}|_{z=0} = \mathbf{q}_0\,\delta(t)$ ($|u_z(\omega)|$, point-dashed line) and for the frequency-domain integrand as a whole ($|u_z(\omega)V(\omega)|$, dashed line).

The signals $u_z(t)$ measured and computed at the points B_m in the case of the presence of obstacles (the second series) are shown in figure 8 ($f_c = f_2 = 100$ kHz, $\omega = 0.20$), while figure 9 presents experimental (left) and theoretical (right) 2D snapshot surface scans of the vertical velocity $\dot{u}_z(x, y, 0, t)$ at $t = 0.16$ μs for the same incident field $\mathbf{u}_0$. At all plots of figure 8 the reflected signal is clearly visible as a small wave packet following after the large incident wave record, though at subplot 8(c) it is interacting with the latter. In figure 9 the reflected field $\mathbf{u}_{sc}$ is visible even better. It manifests itself as concentric circle wave fronts diverging from the point of obstacle location in the backward south-west direction, while there is also visible a shadow zone in the transmitted field behind the obstacle, which stretches in the north-east direction.

A very good coincidence of theoretical and experimental plots and scan-images confirms high prediction ability of the mathematical model developed. It should be remarked that just a small, comparatively simple part of the model has been employed for these predictions, while it could also account for patch-structure interaction and for a higher multimode frequency range [7], as well, as for laminate isotropic [24], anisotropic
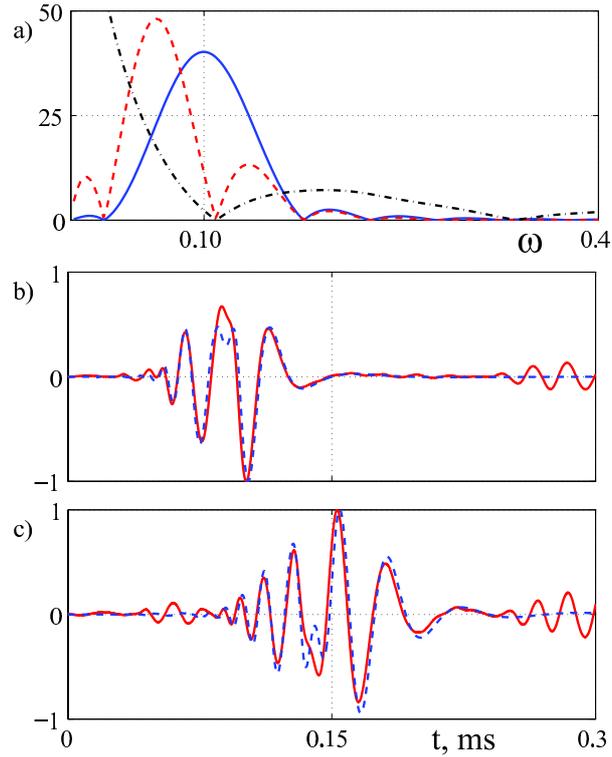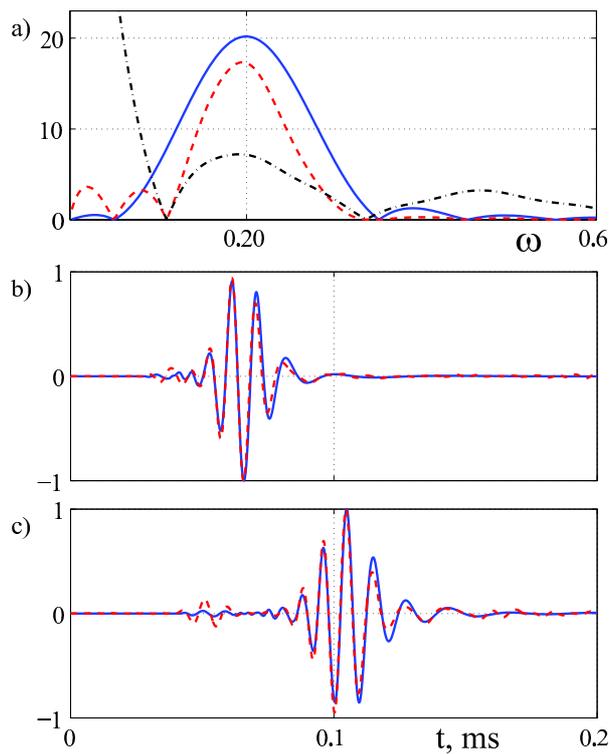
Figure 5. Theoretical (solid lines) and experimental (dashed lines) wave patterns for the aluminium plate excited by a circular piezoactuator at the points A_1 ($r = 70$ mm,(b)) and A_2 ($r = 140$ mm,(c)); subplot (a) is for frequency spectra $|V(\omega)|$ (solid line), $|u_z(\omega)|$ (point-dashed line) and $|u_z(\omega)V(\omega)|$ (dashed line).

[25] and functionally graded elastic properties of the substrate. The obstacles may be not only on the surface but also hidden ones, such as arbitrarily shaped and inclined cracks [18, 26], inclusions and cavities [24], and so far.

4.2. Proper choice of central excitation frequencies

In the Lamb wave based SHM there are two main sensing techniques: first, by piezo patch sensors and, second, using laser vibrometers. To demonstrate their specific features and difference in results provided by these two ways, let us consider frequency spectra of the registered a_0 (solid lines) and s_0 (dashed lines) modes generated by the same circle patch generator ($a = 8$ mm) as in the examples above (figure 10). The upper subplot is for the laser-measured vertical displacement amplitude $|u_z(\omega)|$ calculated in the point A_1 ($r = 70$ mm), while the low one depicts the response $|V_c(\omega)|$ of a piezosensor centered at the same point A_1. The voltage V_c of received signals has been computed using the equality [27]
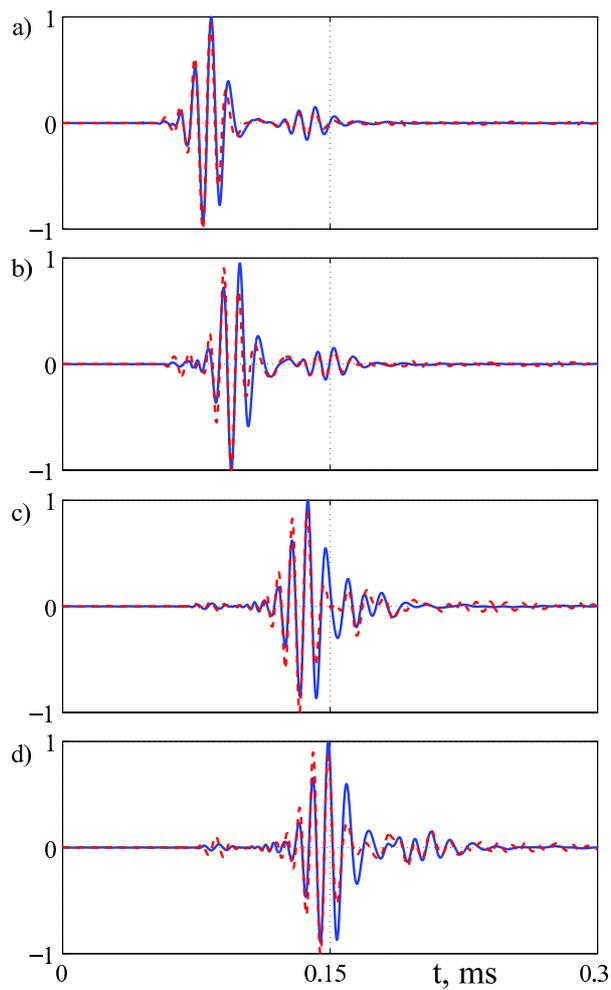
$$V_c = \frac{A_c}{S_c} \iint\limits_{\Omega_c} \left(\frac{\partial u_x}{\partial x} + \frac{\partial u_y}{\partial y} \right) dx dy,$$
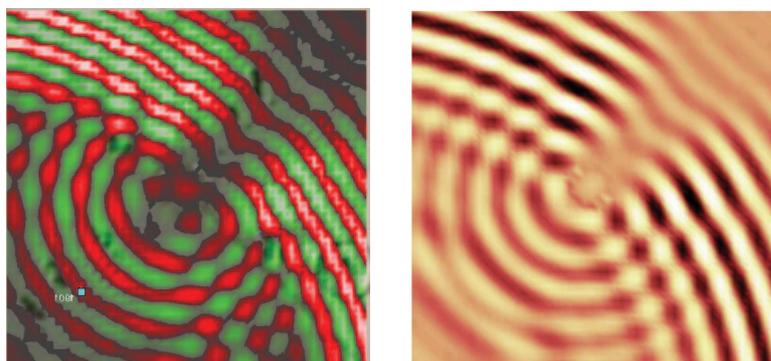
Figure 6. The same as in figure 5 but for $f_c = 100$ kHz.
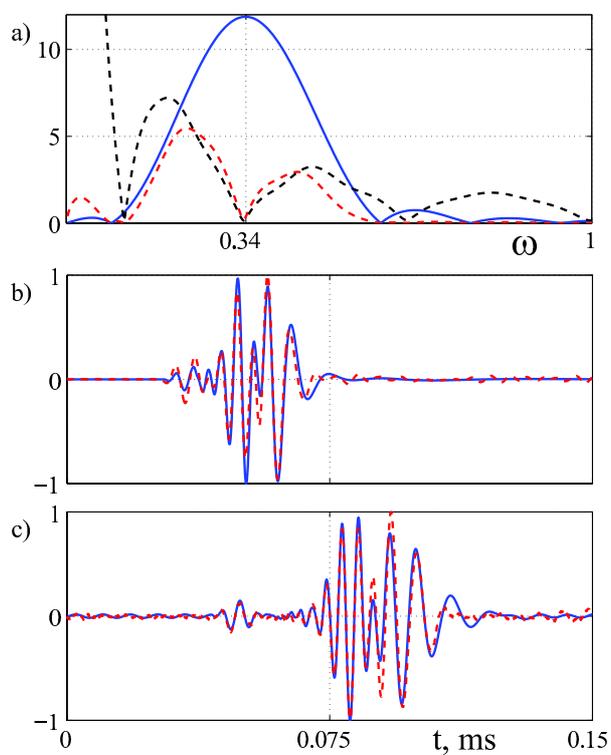
**Figure 7.** The same as in figure 5 but for $f_c = 170$ kHz.

Figure 8. Theoretical (solid lines) and experimental (dashed lines) signals received at the points B_m on the plate with obstacles (see figure 1).

Figure 9. Experimental (left) and computed (right) snap-shot scans of the vertical velocity component $u_z(x, y, 0, t)$ for the wave field diffracted by the obstacle; $f_c = 100$ kHz, $t = 0.16$ μs.

where u_x and u_y are components of the generated field $\mathbf{u}_0$ considered in the sensor contact area $\Omega_c : (x - x_c)^2 + (y - y_c)^2 < a^2$, $x_c = 70$ mm, $y_c = 0$, $a = 8$ mm; $S_c = \pi a^2$ is the area of Ω_c and A_c, which depends on electrical and mechanical properties of the sensor, is taken to be equal to unity.
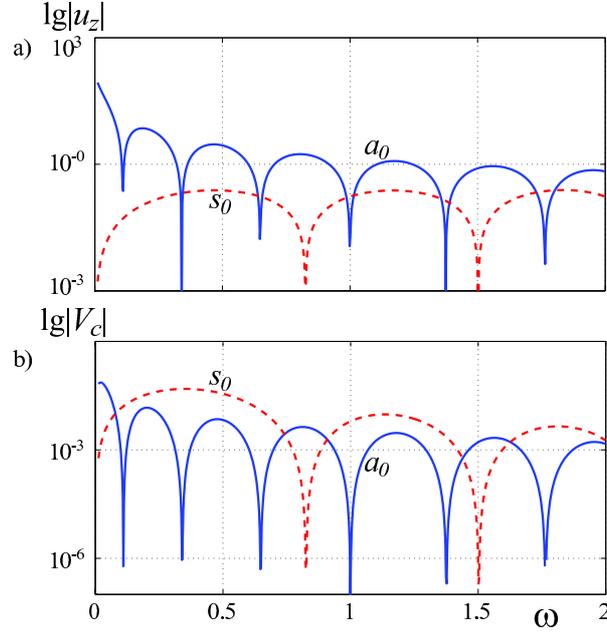
Figure 10. Frequency spectra of the laser-sensed out-of-plane displacement $|u_z|$ (subplot (a)) and of the piezo-sensed voltage $|V_c|$ (subplot (b)) for a_0 (solid line) and s_0 (dashed line) modes.

Predictably, first of all the laser-based sensing registers the a_0 mode (figure 10(a)), while the piezo patch sensor gives a stronger response to s_0 mode than to a_0 one (figure 10(b)). Consequently, the frequencies at which $|V_c|$ for s_0 signals reaches local maximums, (e.g., at $\omega_3 = 0.34$ or $f_3 = 170$ kHz in the example considered) have been named 'sweet spots' of PZT SHM [4, 12]. They should be chosen as the central frequencies f_c for a driving voltage (4.1). Naturally, these frequencies may not be optimal for the u_z laser registration. Moreover, in the example considered $\omega_3 = 0.34$ hits upon the minimum of a_0 amplitude conditioned by eq. (3.19). It results not only in worse conditions for laser detection, but also in essential disturbances complicating accurate interpretation of the patch-sensed reflected signals, due to the fact that instead of one strong maximum of the driven voltage spectrum $|V(\omega)|$ the total spectrum $|V(\omega)u_z(\omega)|$ has two local maximums at $\omega = 0.23$ and $\omega = 0.44$ ($f = 114$ and $f = 219$ kHz) (figure 7(a)). Therefore, the wave package becomes blurred (figures 7(b) and 7(c)) separating at longer distances into two packages (figure 11) propagating with different group velocities $c_{g,1} = 1881$ and $c_{g,2} = 2369$ m/s (figure 2).

Local maximums of $|u_z(\omega)|$ (a_0 sweet spots) look more attractive for laser-based sensing since they do not yield dispersive wave packets. For example, the wave packet excited by the four-cycled Hann windowed sine toneburst at the central frequency
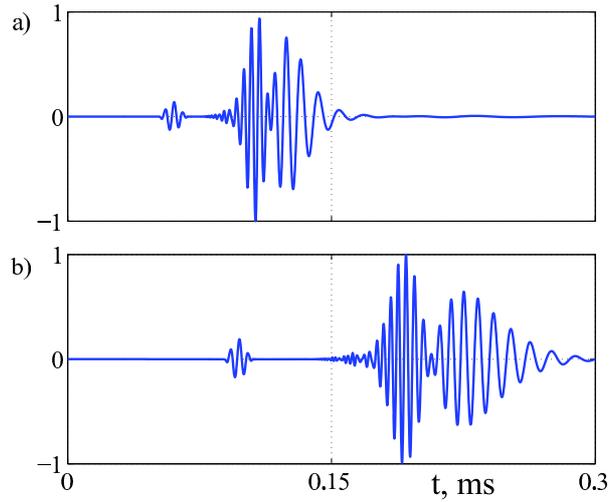
Figure 11. The same as in figure 7 but for the points A_3 and A_4.

$f_c = f_4 = 233$ kHz ($\omega_4 = 0.49$) which hits upon the second local maximum of $|u_z|$ (figure 12(a)), propagates without visible dispersion (figures 12(b) and 12(c)) that enables high quality resolution of defects detected by the reflected field. On the contrary, the reflected from the obstacle signals, excited with $f_c = 50$ kHz and $f_c = 170$ kHz (the spectrum see in figures 5(a) and 7(a)) and calculated in the point B_1 (figure 13) are fuzzy.
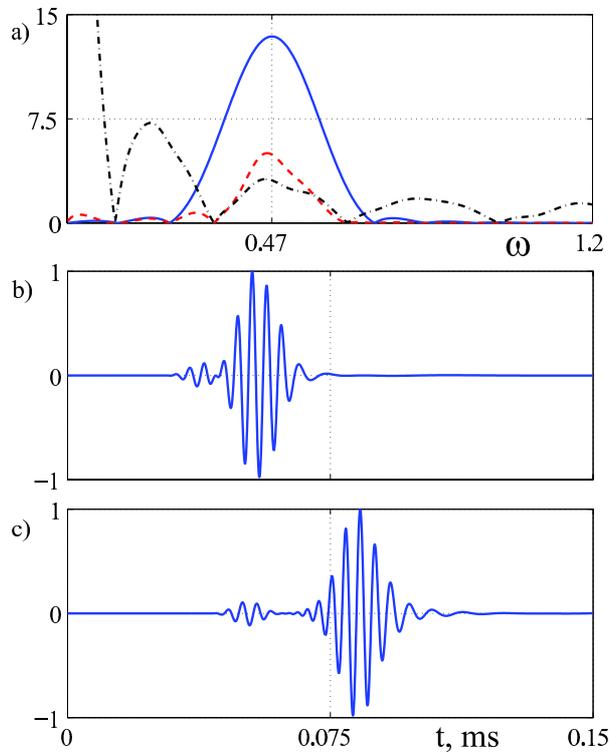
Figure 12. The same as in figure 5 but for $f_c = 233$ kHz (non-dispersive signal).
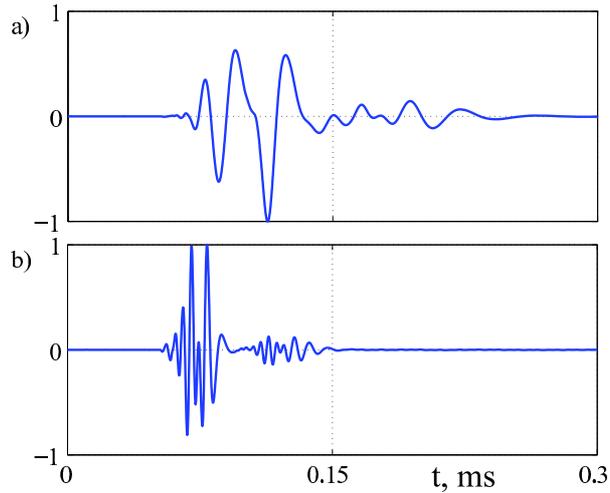
Figure 13. Theoretical wave patterns at point B_1 in the plate with obstacles; $f_c = 50$ kHz (a) and $f_c = 170$kHz (b) (dispersive wave packets).

5. Conclusion

The analytically-based computer model developed for the simulation of Lamb wave excitation, propagation and diffraction in laminate structures (composite plates) with obstacles (defects) is a convenient tool for the interpolation of measured data and for the elaboration of smart algorithms for defect detection and characterization. In particular, it has been demonstrated that the sweet spot central frequencies, proposed for optimal s_0 mode based SHM, may be improper for a laser-based sensing. As a proper choice for a laser-based sensing, it is suggested to use tonebursts with central frequencies f_c providing maximal values of the structure response spectrum $|u_z(\omega)|$, i.e. those located between the points of its local minimums conditioned by eq. (3.19) (for a circle actuator). The response spectra for patch actuators of other shape (e.g. for rectangle ones) can be easily obtained in the context of the model developed including with strict accounting for patch-structure interaction via the contact problem solution. It paves the way for making tables of optimal central frequencies for given plate samples and actuating tools.

6. Acknowledgements

References

[1] Lowe M J S and Diligent O 2001 Low-frequency reflection characteristics of the s_0 Lamb wave from a rectangular notch in a plate *J. Acoust. Soc. Am.* **111** 64–74

[2] Rajagopal P and Lowe M J S 2007 Short range scattering of the fundamental shear horizontal guided wave mode normally incident at a through-thickness crack in an isotropic plate *J. Acoust. Soc. Am.* **122**(3) 1527–38

[3] Staszewski W J, Lee B C and Traynor R 2007 Fatigue crack detection in metallic structures with Lamb waves and 3D laser vibrometry *Meas. Sci. Technol.* **18** 727-39

[4] Giurgiutiu V 2007 Structural Health Monitoring with Piezoelectric Wafer Active Sensors. *Academic Press, London.*

[5] Crawley E F and de Luis J 1987 Use of piezoelectric actuators as elements of intelligent structures *AIAA J.* **25** 1373-85

[6] Wang X D and Huang G L 2001 Wave propagation in electromechanical structures: induced by surface-bonded piezoelectric actuators *J. Intell. Mater. Syst. Struct.* **12** 105-15

[7] Glushkov E, Glushkova N, Kvasha O and Seemann W 2007 Integral equation based modeling of the interaction between piezoelectric patch actuators and an elastic substrate *Smart Mater. Struct.* **16** 650–64

[8] Raghavan A and Cesnik C E S 2005 Finite-dimensional piezoelectric transducer modeling for guided wave based structural health monitoring *Smart Mater. Struct.* **14** 1448–61

[9] Salas K I and Cesnik C E S 2009 Guided wave excitation by a CLoVER transducer for structural health monitoring: theory and experiments *Smart Mater. Struct.* **18** 27

[10] von Ende S and Lammering R 2007 Investigation on piezoelectrically induced Lamb wave generation and propagation *Smart Mater. Struct.* **16** 1802–09

[11] Giurgiutiu V 2003 Lamb wave generation with piezoelectric wafer active sensors for structural health monitoring *Proc. SPIE on Smart Structures and Materials* V. 5056 111-22

[12] Giurgiutiu V 2005 Tuned Lamb wave excitation and detection with piezoelectric wafer active sensors for structural health monitoring *J. Intell. Mater. Syst. Struct.* **16** 291-305

[13] Wang X, Lu Y and Tang J 2008 Damage detection using piezoelectric transducers and the Lamb wave approach: I. System analysis *Smart Mater. Struct.* **17**

[14] Staszewski W J, Lee B C, Mallet L and Scarpa F 2004 Structural health monitoring using scanning laser vibrometry: I. Lamb wave sensing *Smart Mater. Struct.* **13** 251–60

[15] Sveshnikov A V 1951 The limit absorption principle for a wave guide, *Dokl. Akad. Nauk SSSR* **80**(3) 345-47 (In Russian)

[16] Glushkov E and Glushkova N 2001 On the efficient implementation of the integral equation method in elastodynamics *Journal of Computational Acoustics* **9**(3) 889–98.

[17] Brebbia C A, Telles J C F, and Wrobel L C 1984 Boundary Element Techniques *Springer-Verlag.*

[18] Glushkov E, Glushkova N, Ekhlakov A and Shapar E, 2006 An analytically based computer model for surface measurements in ultrasonic crack detection *Wave Motion* **43**(6), 458–73.

[19] Hertz, H. R. 1882 Über die Berührung fester elastischer Körper (On Contact Between Elastic Bodies), in Gesammelte Werke (Collected Works), Vol. 1, Leipzig, Germany, 1895.

[20] Giurgiutiu V. and Zagrai A.N. 2000 Characterization of piezoelectric wafer active sensors, *Journal of Intelligent Material Systems and Structures* **11**(12) 959–75.

[21] Raghavan, A. and Cesnik, C.E.S. 2007 Review of guided-wave structural health monitoring, *The Shock and Vibration Digest* **39**(2) 91–114.

[22] Abramowitz M, Stegun I A (Eds.) 1970 Handbook of Mathematical Functions, National Bureau of Standards.

[23] Viktorov I A 1967 Rayleigh and Lamb Waves: Physical Theory and Applications *Plenum Press, New York.*

[24] Glushkov Ye V, Glushkova N V, Yeremin A A, Mikhas'kiv V V 2009 The layered element method in the dynamic theory of elasticity *Journal of Applied Mathematics and Mechanics* **73** 449-56.

[25] Glushkov E V, Glushkova N V, Krivonos A S 2010 Excitation and propagation of elastic waves in multilayered anisotropic composites *Journal of Applied Mathematics and Mechanics* **74**.

[26] Glushkov Ye V, Glushkova N V, Golub M V 2007 Diffraction of elastic waves by an inclined crack in a layer *Journal of Applied Mathematics and Mechanics* **71** 643–54.

[27] Raghavan A and Cesnik C E 2005 Piezoelectric-actuator excited-wave field solutions for guided-wave structural health monitoring *Smart Structures and Materials 2005: Sensors and Smart Structures Technologies for Civil, Mechanical, and Aerospace Systems*, Edited by Tomizuka, Masayoshi. Proceedings of the SPIE **5765** 313–23.

7. Appendix

For a stress-free elastic layer of thickness h the functions entering in matrix K (3.9) are of form:

$$M(\alpha, z) = -i\sigma_2\{\alpha^2\gamma^2(\sigma_1\sigma_2\,s_2 + \gamma^2\,s_1) - \\ -\alpha^2\gamma^4\,cs_{21} + \alpha^4\sigma_1\sigma_2\,sc_{21} - \alpha^2\gamma^2\sigma_1\sigma_2\,cs_{12} + \gamma^6\,sc_{12}\}/(\alpha^2\Delta(\alpha))$$

$$N(\alpha, z) = i\,\mathrm{ch}\,\sigma_2(z+h)/(\mu\alpha^2\sigma_2\,\mathrm{sh}\,\sigma_2 h)$$

$$P(\alpha, z) = \{-\sigma_1\sigma_2(\gamma^2\alpha^2\,c_1 + \gamma^4\,c_2) - \\ -\alpha^2\sigma_1^2\sigma_2^2\,ss_{12} + \sigma_1\sigma_2\gamma^4\,cc_{12} + \alpha^2\sigma_1\sigma_2\gamma^2\,cc_{21} - \gamma^6\,ss_{21}\}/\Delta(\alpha)$$

$$R(\alpha, z) = \sigma_1\{-\alpha^2\gamma^2(\sigma_1\sigma_2\,s_1 + \gamma^2\,s_2) + \\ +\alpha^2\sigma_1\sigma_2\gamma^2\,cs_{21} - \gamma^6\,sc_{21} + \alpha^2\gamma^4\,cs_{12} - \alpha^4\sigma_1\sigma_2\,sc_{12}\}/\Delta(\alpha)$$

$$S(\alpha, z) = -i\{\sigma_1\sigma_2\gamma^2(\alpha^2\,c_2 + \gamma^2\,c_1) - \\ -\sigma_1\sigma_2\gamma^4\,cc_{21} + \alpha^2\sigma_1^2\sigma_2^2\,ss_{21} - \alpha^2\sigma_1\sigma_2\gamma^2\,cc_{12} + \gamma^6\,ss_{12}\}/\Delta(\alpha)$$

where

$$\Delta(\alpha) = 2\mu[-2\alpha^2\sigma_1\sigma_2\gamma^4 - (\gamma^8 + \alpha^4\sigma_1^2\sigma_2^2)\,\mathrm{sh}\,\sigma_1 h\,\mathrm{sh}\,\sigma_2 h + 2\alpha^2\sigma_1\sigma_2\gamma^4\mathrm{ch}\,\sigma_1 h\,\mathrm{ch}\,\sigma_2 h]$$

$$s_n = \mathrm{sh}\sigma_n z, \quad c_n = \mathrm{ch}\sigma_n z, \quad \gamma^2 = \alpha^2 - 0.5\kappa_2^2$$
$$ss_{mn} = \mathrm{sh}\sigma_m h\,\mathrm{sh}\sigma_n(z+h), \quad cs_{mn} = \mathrm{ch}\sigma_m h\,\mathrm{sh}\sigma_n(z+h)$$
$$sc_{mn} = \mathrm{sh}\sigma_m h\,\mathrm{ch}\sigma_n(z+h), \quad cc_{mn} = \mathrm{ch}\sigma_m h\,\mathrm{ch}\sigma_n(z+h)$$
$$\sigma_n = \sqrt{\alpha^2 - \kappa_n^2}, \quad \kappa_1^2 = \rho\omega^2/(\lambda+2\mu), \quad \kappa_2^2 = \rho\omega^2/\mu, \quad m, n = 1, 2$$